Superexchange interaction in the *A*-site ordered perovskite $YMn_3Al_4O_{12}$

Masayuki Toyoda,[1,2,*] Takashi Saito,[3] Kunihiko Yamauchi,[2] Yuichi Shimakawa,[3,4] and Tamio Oguchi[2,1]
[1]*CREST, Japan Science and Technology Agency, 8-1, Mihogaoka, Ibaraki, Osaka 567-0047, Japan*
[2]*Institute of Scientific and Industrial Research, Osaka University, 8-1, Mihogaoka, Ibaraki, Osaka 567-0047, Japan*
[3]*Institute for Chemical Research, Kyoto University, Uji, Kyoto 611-0011, Japan*
[4]*CREST, Japan Science and Technology Agency, Uji, Kyoto 611-0011, Japan*
(Received 21 April 2015; revised manuscript received 4 June 2015; published 22 July 2015)

Crystal structure and magnetic ordering in $YMn_3Al_4O_{12}$ are determined by neutron powder diffraction measurement, indicating that $S = 2$ spins of the A'-site Mn^{3+} ions are ordered in G-type antiferromagnetic (AFM) arrangement in the $Im\bar{3}$ cubic crystal structure. Using the first-principles electronic structure calculations, it is found that the AFM spin structure is stabilized by the nearest-neighbour (NN) exchange interaction. The underlying mechanism of the NN exchange is revealed to be the antiferromagnetic Mn-O-Mn superexchange interaction from the calculations of electronic transfer integrals.

DOI: 10.1103/PhysRevB.92.014420 PACS number(s): 75.25.−j, 75.50.Ee, 71.15.Mb, 75.30.Et

I. INTRODUCTION

A-site ordered perovskite oxides $AA'_3B_4O_{12}$ have recently attracted increasing attention because they exhibit a wide variety of interesting chemical and physical properties [1]. Magnetism in these materials is of particular interest because they can contain transition-metal ions both at the A' and B sites. The sublattice formed by the A' sites is a 1/4 depleted cubic lattice and the oxygen local geometry around each site is in square-planer D_{4h} symmetry [2], both showing significant difference from the conventional geometry of the B site sublattice.

Let us take $YMnO_3$ and $YMn_3Al_4O_{12}$ as examples to illustrate the difference between the A'- and the B-site sublattices. In $YMnO_3$, Mn^{3+} ions occupy the B sites. The d^4 electronic configuration is Jahn-Teller (JT) active in the O_h crystal field. Due to the orbital order caused by the JT distortion, $YMnO_3$ crystallizes in an orthorhombic $Pnma$ structure ($\sqrt{2}a_p \times 2a_p \times \sqrt{2}a_p$ superstructure where a_p is the edge dimension of ideal cubic perovskite structure) [3]. $YMn_3Al_4O_{12}$, which has been recently synthesized by Tohyama and coworkers [4], contains Mn^{3+} ions at the A' sites and crystallizes in a cubic $Im\bar{3}$ ($2a_p \times 2a_p \times 2a_p$) structure as shown in Fig. 1, where Mn^{3+} in the D_{4h} local symmetry is no longer JT active. Because of such geometrical differences, they exhibit different ordering patterns of the Mn-3*d* states. In $YMnO_3$, the distortion and rotation of MnO_6 octahedra determines the ordering of the singly occupied e_g orbital states. According to the Goodenough-Kanamori-Anderson (GKA) rule [5–7], the orbital ordering suppresses the nearest-neighbor (NN) exchange interaction but enhances the second-NN exchange interaction, resulting in the E-type antiferromagnetic (AFM) spin ordering below 42 K [8,9]. In $YMn_3Al_4O_{12}$, on the other hand, the MnO_4 plaquettes determine the ordering of the Mn-3*d* orbital states. Since the plaquettes have different orientations as shown in Fig. 1, the ordering pattern is expected to be much more complex than the $YMnO_3$ case. It has been experimentally confirmed that $YMn_3Al_4O_{12}$ undergoes an AFM transition at 35 K [4], while the ground-state spin structure has not been clarified yet. As the origin of the magnetic exchange interaction, Mn-Mn direct exchange [4] and Mn-O-O-Mn supersuperexchange [10] have been suggested by several authors, though it remains controversial.

The present work was conducted aiming to elucidate the detailed spin structure and the underlying magnetic exchange interaction in $YMn_3Al_4O_{12}$. In contrast to the magnetism with the perovskite B sites that has been extensively and comprehensively studied for decades, magnetic interactions between the cations on the perovskite A (or A') sites still requires investigation. An understanding of them would also be necessary for the study of more complex materials containing magnetic transition metals both at the A' and B sites, such as $CaMn_7O_{12}$ that shows magnetoelectric coupling [11] and $BiCu_3Mn_4O_{12}$ that is magnetoresistive [12]. $YMn_3Al_4O_{12}$ is particularly suitable for the purpose as it contains nonmagnetic aluminum at the B site. In the following sections, the detailed spin structure of $YMn_3Al_4O_{12}$ is determined by a neutron powder diffraction measurement and the magnetic exchange interaction is theoretically studied by using first-principles electronic structure calculations.

II. EXPERIMENT

A polycrystalline sample of $YMn_3Al_4O_{12}$ was synthesized under a high-pressure and high-temperature condition [13]. Powdered Y_2O_3, Mn_2O_3, and Al_2O_3 were ground in a mortar and packed into a gold capsule. The mixture was heated up to 1173 K, held for 1 h at that temperature, and slowly cooled down to room temperature during the next 5 h, under a pressure of 9 GPa in a cubic anvil press. The AFM transition at $T_N = 35$ K was confirmed by a magnetic susceptibility measurement, as reported previously [4]. Neutron powder diffraction experiments on the polycrystalline sample were performed at the diffractometer D20 (Institut Laue Langevin, France) in its high-intensity mode, at temperatures between 5 and 300 K, with a neutron wavelength of 2.41 Å. The sample was placed in a vanadium can of 4 mm diameter and mounted in a standard cryostat. Rietveld refinements of the diffraction patterns were carried out using the FULLPROF program [14], which allows simultaneous refinement of the structural and magnetic parameters.

*toyoda-cmp@sanken.osaka-u.ac.jp

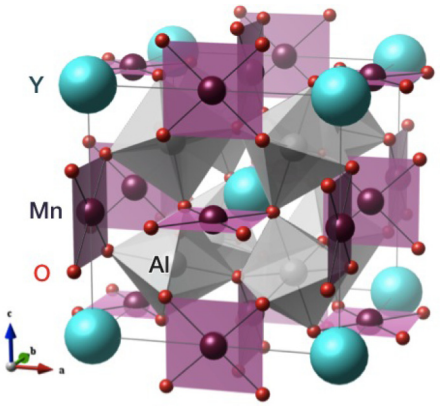

FIG. 1. (Color online) Crystal structure of $YMn_3Al_4O_{12}$.

III. THEORY

A. Electronic structure calculations

The electronic structure of $YMn_3Al_4O_{12}$ was calculated based on the first-principles density functional theory (DFT). The Vienna *ab initio* simulation package (VASP) was used [15–20]. The cut-off energy for the plane wave expansion was 500 eV. The electronic exchange and correlation was described within the generalized gradient approximation by using the functional parameterized by Perdew, Burke, and Ernzerhof (GGA-PBE) [21]. The GGA+U approach was also used to take into account the localized nature of the Mn-3d electrons. The effective on-site Coulomb repulsion is chosen to be $U_{\rm eff} = 4.5$ eV from the linear-response estimation for $LaMnO_3$ [22]. An $8 \times 8 \times 8$ Monkhorst-Pack k-point grid [23] was used to sample the Brillouin zone. The crystal structure was fully optimized with respect to the lattice parameters and internal atomic coordinates until the remaining forces were less than 1 meV/Å.

A tight-binding model was used to analyze the calculated electronic structure. To extract the tight-binding parameters, the maximally localized Wannier functions (MLWFs) for Mn-d and O-p states were calculated by using the WANNIER90 package [24,25]. A set of N Wannier functions $|w_{n\boldsymbol{R}}\rangle$ specified by band index n and lattice vector $\boldsymbol{R}$ are defined as the Fourier transform of N bands of Bloch functions $|\psi_{m\boldsymbol{k}}\rangle$ specified by band index m and wave vector $\boldsymbol{k}$,

$$|w_{n\boldsymbol{R}}\rangle = \frac{V}{(2\pi)^3}\int_{\rm BZ}\left[\sum_{m=1}^{N} U_{mn}^{(\boldsymbol{k})}|\psi_{m\boldsymbol{k}}\rangle\right]e^{-i\boldsymbol{k}\cdot\boldsymbol{R}}d\boldsymbol{k}, \quad (1)$$

where $U_{mn}^{(\boldsymbol{k})}$ is a unitary transformation matrix that mixes bands at the wave vector $\boldsymbol{k}$. The MLWFs are obtained by minimizing the spatial spread of the Wannier functions with respect to $U_{mn}^{(\boldsymbol{k})}$. The intersite Hamiltonian matrix elements in a basis of the Wannier functions correspond to the transfer integrals that are used in the tight-binding model,

$$t_{\boldsymbol{R}\boldsymbol{R}'}^{nn'} \equiv \langle w_{n\boldsymbol{R}}|\hat{H}|w_{n'\boldsymbol{R}'}\rangle = \frac{V}{(2\pi)^3}\int_{\rm BZ}\sum_{m}\left(U_{mn}^{(\boldsymbol{k})}\right)^{*}\epsilon_{m\boldsymbol{k}}U_{mn'}^{(\boldsymbol{k})}e^{i\boldsymbol{k}\cdot(\boldsymbol{R}-\boldsymbol{R}')}d\boldsymbol{k}, \quad (2)$$

where $\epsilon_{m\boldsymbol{k}}$ is the eigenvalue of the Bloch state $|\psi_{m\boldsymbol{k}}\rangle$.

B. Heisenberg model

The magnetic exchange interactions between the A'-site spin moments were studied using a Heisenberg-type model Hamiltonian $E = -\sum_{i<j} J_{ij}\boldsymbol{e}_i \cdot \boldsymbol{e}_j$, where J_{ij} is the exchange coupling parameters and e_i a unit vector pointing to the direction of the spin moment at site i. The magnitude of the spins is effectively included in J_{ij}. As we assume that the magnetic ordering is collinear and the exchange interaction is isotropic, we can classify spin pairs into each shell of NN spins, so that the Hamiltonian is rewritten by taking summation within each shell: $E = -\sum_l (n_l^+ - n_l^-)J_l$, where $n_l^{+(-)}$ is the number of parallel (antiparallel) spin pairs and J_l the average exchange coupling for the lth NN shell. Since $YMn_3Al_4O_{12}$ is an insulator, the exchange interaction is expected to be of short range. If the exchange interaction is mediated by B-site Al, the exchange interaction between the second- and the third-NN shells may also be strong because they are connected by a single BO_6 octahedron (see Fig. 1). Any interaction longer than the third-NN interaction should be less significant because it has to be mediated by multiple BO_6 octahedra. Therefore, the l summation was taken up to $l = 3$,

$$E \approx -\sum_{l=1}^{3}(n_l^+ - n_l^-)J_l, \quad (3)$$

and longer-range interactions were ignored in this paper.

Since $n_l^{\pm}$ is geometrically determined for given lattice and spin structures, the exchange couplings J_l can be estimated from the DFT total energies that are obtained with constraints on the spin configurations. In the actual calculations to estimate the exchange couplings, four different collinear spin structures were considered. The detailed procedure of the estimation is described in a previous article [26]. The AFM transition temperature was calculated as

$$T_{\rm N}^{\rm DFT-MFA} \approx \frac{4}{3k_B}(-J_1 + 2J_2 - 2J_3), \quad (4)$$

within the mean-field approximation (MFA).

IV. RESULTS

Figure 2 shows the temperature evolution of the diffraction patterns. All the observed reflections from the sample above

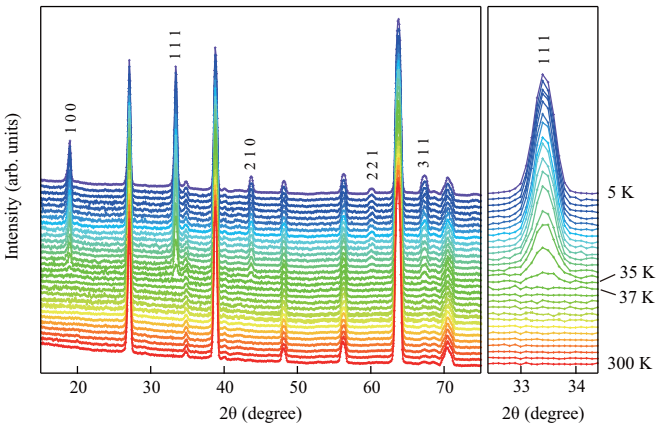

FIG. 2. (Color online) Temperature evolution of the neutron diffraction patterns of $YMn_3Al_4O_{12}$ from 5–300 K.

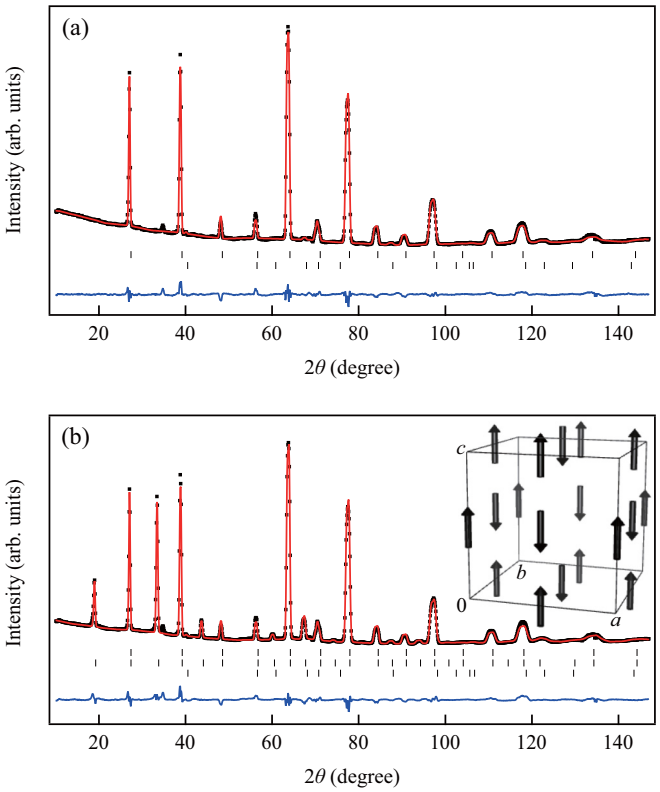

FIG. 3. (Color online) Rietveld plots of neutron powder diffraction patterns at (a) 300 K and (b) 5 K. The observed (+), calculated (solid line) and differences (bottom) patterns are shown. The ticks indicate the allowed Bragg reflections for nuclear lattice (above), magnetic (middle, 5 K), and Al_2O_3 impurity (below).

37 K could be indexed with a cubic $Im\bar{3}$ unit cell compatible with the room temperature crystal structure analyzed with the synchrotron diffraction data in our previous study [4]. The result of the Rietveld analysis is shown in Fig. 3(a) and the refined structural parameters, selected bond distances, and bond angles at 300 K are summarized in Tables I and II. The rather large values of the refined B_{iso} can be due to the limitation of the observed Q range ($Q < 0.32$ Å^{-1}), as a result maximizing the neutron flux for the magnetic structure analysis. About 7% of Mn was detected at the B site, consistent with the presence of a small amount of Al_2O_3 impurity. No trace of Al inclusion was detected at the A' site. The bond valence sums of the A-site Y, A'-site Mn, and B-site Al are, respectively, 2.97, 2.98, and 2.82, confirming the $Y^{3+}Mn_3^{3+}Al_4^{3+}O_{12}$ charge state and also being in good agreement with the previous study [4].

On the other hand, new reflections breaking the I-centered symmetry of the high-temperature structure, such as 1 0 0, 1 1 1, and 2 1 0, appear below $T_N = 35$ K. These additional intensities below T_N are well reproduced with a G-type AFM spin arrangement of the A'-site Mn spins. The result of fitting the data at 5 K is shown in Fig. 3(b), and the obtained spin structure is illustrated in the inset of Fig. 3(b). The refined structural parameters and selected bond distances and bond angles at 5 K are summarized in Tables I and II. The rather small Q range described above should not affect the magnetic structure analysis, since the magnetic Bragg reflections are observed only in the low-Q region. The refined magnetic moment of the Mn site at 5 K is 2.92(2)μ_B, and the temperature dependence is shown in Fig. 4. The value is rather small compared to 4 μ_B expected for a high spin Mn^{3+} with $S = 2$. This discrepancy can be partly due to the covalency of the Mn-O bonds. No anomaly was found in the temperature dependence of the refined structural parameters, bond distances, and bond angles over the whole temperature range, suggesting the absence of any structural phase transition down to 5 K. The coordination of Mn by O at 5 K is almost identical to that at 300 K; four long bonds of 1.924(2) Å, two rather long bonds of 2.693(2) Å, and two very long bonds of 3.156(2) Å, forming a square planar coordination.

TABLE I. Results of the Rietveld refinement of the neutron powder diffraction (NPD) data for $YMn_3Al_4O_{12}$ at 300 and 5 K. The atom positions are: Y 2a (0, 0, 0), Mn 6b (0, 1/2, 1/2), Al 8c (1/4, 1/4, 1/4), and O 24g (0, y, z). A small amount of Mn inclusion [7.2(6)%] at the Al 8c site was detected by the refinement. The magnetic moment M at the Mn site was refined using the G-AFM spin structure for the 5 K data. Corresponding values calculated by DFT calculations are also shown.

	NPD		DFT	
	$T = 300$ K	$T = 5$ K	GGA	GGA+U
a/Å	7.17967(6)	7.17224(6)	7.232	7.249
y(O)	0.1811(3)	0.1808(3)	0.1800	0.1814
z(O)	0.3025(3)	0.3022(3)	0.3030	0.3020
B_{iso}(Y)/Å^2	3.7(1)	3.9 (1)	–	–
B_{iso}(Mn)/Å^2	4.1(1)	4.1 (1)	–	–
B_{iso}(Al)/Å^2	2.8(2)	2.7 (1)	–	–
B_{iso}(O)/Å^2	8.0(1)	7.3 (1)	–	–
M(Mn)/μ_B	–	2.92(2)	3.64	3.88
R_{wp}/%	5.70	6.69	–	–
R_{nux}/%	4.53	5.72	–	–
R_{mag}/%	–	14.6	–	–

TABLE II. Selected bond distances and bond angles of $YMn_3Al_4O_{12}$. The neutron powder diffraction (NPD) data at 300 and 5 K as well as those obtained by DFT calculations in GGA and GGA + U are shown.

	NPD		DFT	
	$T = 300$ K	$T = 5$ K	GGA	GGA+U
Bond distances/Å				
Y-O	2.531(1)	2.526(1)	2.549	2.553
Mn-O	1.924(2)	1.922(2)	1.930	1.947
Mn-O	2.693(2)	2.693(1)	2.718	2.719
Mn-O	3.166(2)	3.153(2)	3.188	3.182
Mn-Mn	3.58984(3)	3.58612(3)	3.616	3.624
Al-O	1.900(2)	1.898(2)	1.916	1.917
Bond angles/degree				
Al-O-Al	141.8(1)	141.8(1)	141.29	142.01
Al-O-Mn	108.8(1)	108.8(1)	109.02	108.67
Mn-O-Mn	100.8(1)	100.6(1)	100.80	100.62

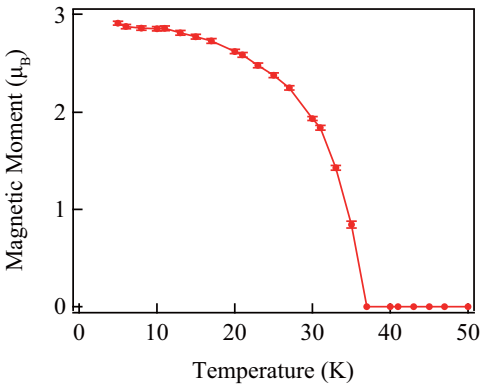

FIG. 4. (Color online) Experimental temperature dependence of the refined magnetic moment at the Mn site.

The observed stable lattice and spin structures of $YMn_3Al_4O_{12}$ were confirmed by the DFT calculations. The total energy is lower in G-type AFM than in a ferromagnetic spin structure both within GGA and GGA+U. The optimized crystal structure has the $Im\bar{3}$ symmetry. The structural parameters are summarized in Tables I and II, showing reasonable agreements with experiments. The calculated magnetic moment is close to the ideal 4 μ_B. In the following, only the GGA+U results are discussed since no qualitative difference is found between the GGA and GGA+U results. Figure 5(a) shows the calculated electronic structure. The valence state consists mainly of Mn-3d and O-2p states. The Mn-3d state is almost completely spin polarized. The majority-spin Mn-3d states are occupied and forming a wide band, except for the $3d_{x^2-y^2}$ orbital state that is unoccupied and appears as a sharp peak at 2.8 eV above the valence band maximum (VBM). (The orbital labels for Mn-d and O-p states are defined according to the local symmetry of the MnO_4 plaquettes [27].) The empty minority-spin Mn-3d manifold is found around 4–5 eV above VBM. The density of states (DOS) is consistent with the observed charge state, i.e., the A'-site Mn ions are in the trivalent state with high-spin d^4 electronic configuration.

The estimated magnetic exchange coupling parameters J_1, J_2, and J_3 are shown in Table III. All the interactions are negative (which favors antiparallel-spin orientations by definition). Since the magnitude of J_1 is much larger than the others, the experimentally observed G-type AFM spin structure is explained by the almost sole contribution of the NN interaction. The Néel temperature $T_N^{\mathrm{DFT-MFA}} = 53.5$ K calculated by Eq. (4) is slightly higher than the experimental value (35 K), which may be due to MFA and related to the fact that the magnetic moment is also larger in the calculation.

V. DISCUSSION

Let us now consider the microscopic mechanism behind the AFM exchange interaction J_1. Based on the calculated Kohn-Sham band structure, the MLWFs were constructed for the valence (both occupied and unoccupied) Mn-3d and O-2p states to extract the intersite d-d, p-d, and p-p electron transfer integrals. Using the tight-binding Hubbard model, AFM direct

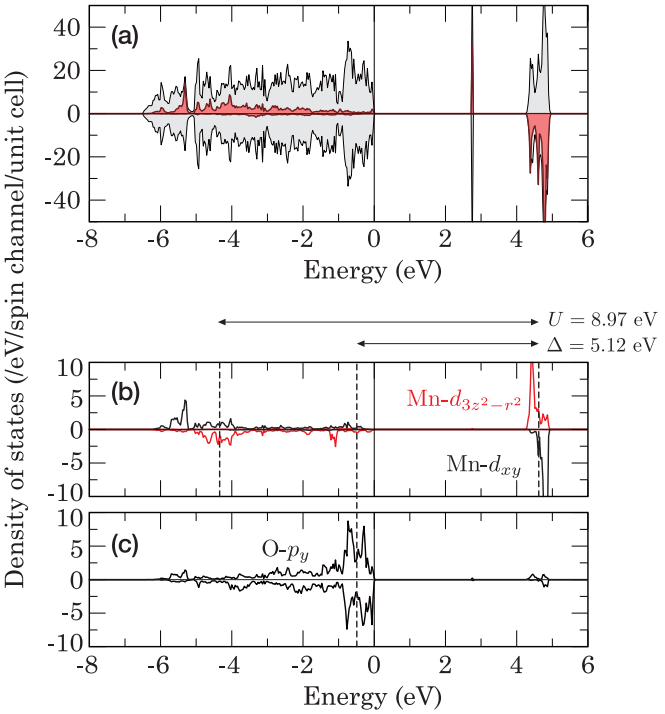

FIG. 5. (Color online) Density of states (DOS) of $YMn_3Al_4O_{12}$ calculated in GGA+U ($U_{\mathrm{eff}} = 4.5$ eV). In (a), the total DOS and Mn partial DOS are shown by the gray and red area, respectively. In (b) and (c), the orbital-decomposed DOS is shown for Mn-$d_{3z^2-r^2}$, Mn-d_{xy}, and O-p_y orbitals that are related to Mn-O-Mn AFM superexchange interaction (see text). The vertical dashed line shows the center of gravity of the upper Hubbard band, lower Hubbard band, and the O-p main peak.

exchange coupling energy is given by

$$J_{\mathrm{DX}} = -\frac{t^2}{U_{dd}}, \tag{5}$$

where t is the transfer integral and U_{dd} the on-site Coulomb repulsion for d states. The Kramers-Anderson-type superexchange coupling energy [29] is

$$J_{\mathrm{SX}} = -\frac{t^4}{\Delta_{pd}^2}\left(\frac{1}{\Delta_{pd}} + \frac{1}{U_{dd}}\right), \tag{6}$$

where Δ_{pd} is the p-d charge-transfer integral. In general, magnetism in transition-metal oxides is explained by superexchange rather than direct exchange because the 3d electrons are well localized compared to interatomic distances. However, in the A-site ordered perovskite structure, there is no oxygen atom between the NN A'-site cations and thus paths for superexchange are not obviously found. In fact, Li and coworkers

TABLE III. Estimated magnetic exchange coupling parameters of $YMn_3Al_4O_{12}$ from DFT calculations with GGA+U.

Shell	$l = 1$	$l = 2$	$l = 3$
J_l (meV)	− 2.52	− 0.12	− 0.59
$J_l/(J_1)$	− 1	− 0.046	− 0.23

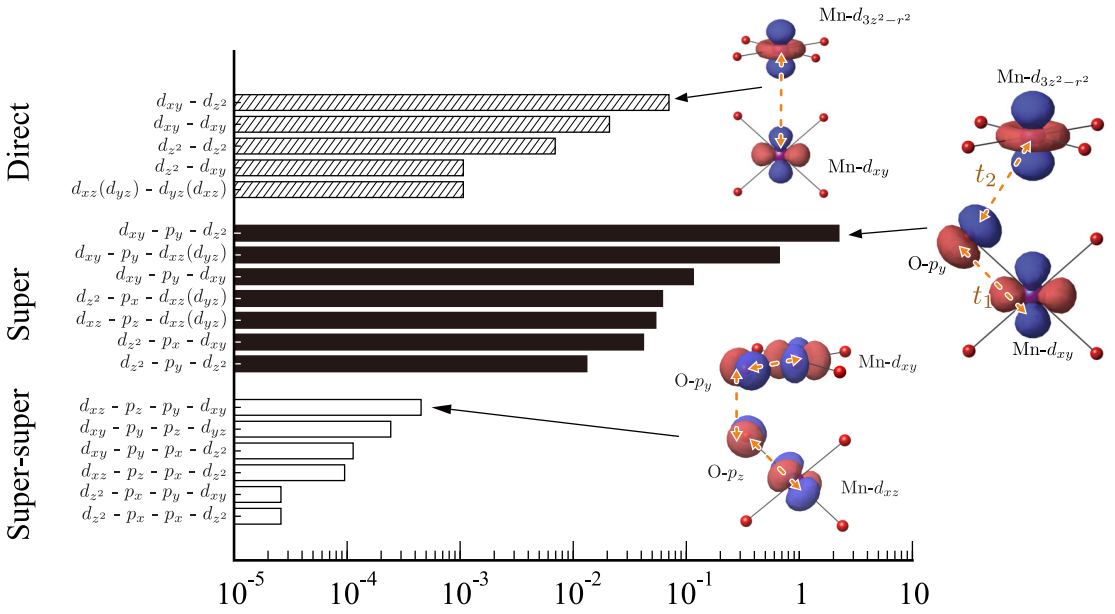

FIG. 6. (Color online) Absolute values of calculated exchange interaction energies for direct exchange, superexchange, and super-superexchange based on the tight-binding Hubbard model. Note that the horizontal axis is in logarithmic scale. The transfer integrals were numerically calculated using the MLWFs. The Hubbard parameters ($\Delta_{pd} = 4.5$ eV and $J_{dd} = 7.5$ eV) were taken from the experimental values for $LaMnO_3$ [28].

[10] suggested a possible contribution from the Mn-O-O-Mn supersuperexchange interaction in $YMn_3Al_4O_{12}$ based on their analysis on the charge densities. Such an extended interaction involving two mediating anions has been also discussed on perovskite-type transition-metal oxides in literature, such as the Co-O-O-Co interaction in $BiCoO_3$ [30] and Mn-O-O-Mn interaction in E-type AFM rare-earth manganites [31–33]. Using the same derivation for the conventional superexchange energy (6), the antiferromagnetic supersuperexchange coupling energy is obtained as the sixth-order perturbation energy

$$J_{\mathrm{SSX}} = -\frac{t^6}{\Delta_{pd}^4}\left(\frac{1}{\Delta_{pd}} + \frac{1}{U_{dd}}\right). \tag{7}$$

We used empirical parameters $\Delta_{pd} = 4.5$ eV and $U_{dd} = 7.5$ eV, which are the best fit values to the x-ray photoemission spectrum for $LaMnO_3$ [28]. (We also estimated these values from our DFT results as schematically shown in Figs. 5(b) and 5(c). The values $\Delta_{pd} = 5.12$ eV and $U_{dd} = 8.97$ eV are close to the empirical values.) Figure 6 summarizes the several direct exchange, superexchange, and supersuperexchange interactions. The strongest is (Mn-d_{xy})-(O-p_y)-(Mn-$d_{3z^2-r^2}$) superexchange with $J_{\mathrm{SX}} = -2.23$ meV. The potentially strongest (Mn-d_{xy})-(Mn-$d_{3z^2-r^2}$) direct exchange is much weaker than the superexchange by more than an order of magnitude ($J_{\mathrm{DX}} = -0.07$ meV) because the intersite d-d transfer is weaker than the p-d transfer. The possible (Mn-d_{xz})-(O-p_z)-(O-p_y)-(Mn-d_{xy}) supersuperexchange ($|J_{\mathrm{SSX}}| < 0.001$ meV) is even weaker because of the high cost of the p-d charge-transfer Δ_{pd}. Such an extensive interaction may be important if the value of Δ_{pd} is almost negligible. In $YMn_3Al_4O_{12}$, however, Δ_{pd} is not small due to the D_{4h} crystal field splitting and strong Mn-O hybridization. All these exchange energies add up to $J^{\mathrm{TB}} \approx -4.11$ meV. The sum of the strongest superexchange energies mediated by O-p_y orbital, namely, (Mn-d_{xy})-(O-p_y)-(Mn-$d_{3z^2-r^2}$), (Mn-d_{xy})-(O-p_y)-(Mn-d_{xz}), (Mn-d_{xy})-(O-p_y)-(Mn-d_{yz}), and (Mn-d_{xy})-(O-p_y)-(Mn-d_{xy}), is -3.56 meV, which accounts for 86.6% of J^{TB}.

We thus conclude that the microscopic origin of the G-type AFM spin structure in $YMn_3Al_4O_{12}$ is the NN superexchange interaction. The path of the strongest superexchange is schematically shown in Fig. 6. It involves two kinds of transfer integrals: ($pd\pi$)-type transfer between Mn-d_{xy} and O-p_y (denoted as t_1) and ($pd\sigma$)-type transfer between Mn-$d_{3z^2-r^2}$ and O-p_y (t_2) with Mn-O distance 1.924 Å and 2.693 Å, respectively. In our numerical results, $|t_1| = 0.789$ eV and $|t_2| = 0.452$ eV. ($pd\sigma$)-type t_2 becomes weaker than ($pd\pi$)-type t_1 because of its longer Mn-O distance. This reflects a characteristic feature of the A'-site sublattice; unlike the interconnected BO_6 octahedra, the $A'O_4$ plaquettes are rather isolated from each other. In previous articles [4,10], the superexchange interaction has been precluded as a possible mechanism for the magnetism in $YMn_3Al_4O_{12}$. The main reason of the preclusion was because one of the Mn-O bonds seems to be too long, which is, however, not long enough to make the hopping (t_2) negligible as we found out above.

The same arguments have been made for $CaCu_3Ge_4O_{12}$ and $CaCu_3Sn_4O_{12}$, which are ferromagnets with the same A-site-ordered perovskite structure as $YMn_3Al_4O_{12}$. The ferromagnetism arises exclusively from the A'-site Cu^{2+} and is suggested in several previous papers [1,34–36] to take place due to direct exchange interaction. However, our recent results of first-principles calculations have shown that the Cu-d states are well hybridized with the valence O-p states, indicating that the ferromagnetism should also be explained by the Cu-O-Cu superexchange mechanism [26]. In $YMn_3Al_4O_{12}$, the superexchange takes place between d_{xy} and $d_{3z^2-r^2}$ states that have different symmetry when we consider their overlap with neighboring O-p orbital states (π- and σ-type, respectively).

On the other hand, in $CaCu_3Ge_4O_{12}$ and $CaCu_3Sn_4O_{12}$, it takes place between two neighboring $d_{x^2-y^2}$ states [26] both of which have σ-type overlap with O-p states. The difference in the symmetry of those p-d bondings changes the sign of superexchange interaction, as illustrated by the GKA rule [5–7].

J_1 is predominantly stronger than J_2 and J_3 in $YMn_3Al_4O_{12}$, being distinct from the situation in $YMnO_3$ where J_1 and J_2 compete with each other to stabilize the E-type AFM spin ordering [8,9]. Therefore, we successfully demonstrate the difference of the electronic states in the Mn^{3+} ions with respect to the orbital ordering and the corresponding spin ordering between the cases when they are in the A'- and the B-site sublattices. This also shows striking difference from other AFM A-site ordered perovskites, such as $CaCu_3Ti_4O_{12}$ and $LaMn_3V_4O_{12}$. $CaCu_3Ti_4O_{12}$ also shows G-type AFM spin structure [37]. However, the NN interaction J_1 has been found to be ferromagnetic for the $S = 1/2$ spin of the A'-site Cu^{2+} ions. The ground-state G-type AFM order is actually due to the third-NN interaction J_3 through Cu^{2+}-O^{2-}-Ti^{4+}-O^{2-}-Cu^{2+} path [34,38,39]. It is enabled by the strong hybridization of Ti-3d and O-2p states [26,35], which is not the case with $YMn_3Al_4O_{12}$ because the energy level of the Al states is far from the O-2p states. In the case of $LaMn_3V_4O_{12}$, the A'-site Mn is divalent with high spin $S = 5/2$ state and the B-site V has mixed valence 3.75+. The ground-state spin structure is an unusual noncollinear 60°-spin structure because J_2 and J_3 compete with J_1 [40]. As expected from the theory of superexchange, the magnetic interaction indeed exhibits drastic change in its sign and magnitude depending on the electronic configuration of the A'-site cations. Since it also depends on the distance and the angle of the interaction path, modulations in the A'-O distance or A'-O-A' angle (for example, by applying chemical/physical pressure) may be exploited to enhance the magnetism. The first- and second-NN A'-O distances in $YMn_3Al_4O_{12}$ ($d_{\text{Mn-O}} = 1.924$ and 2.693 Å) are significantly shorter than those in $CaCu_3Ti_4O_{12}$ ($d_{\text{Cu-O}} =$ 1.971 and 2.780 Å) [34] and $LaMn_3V_4O_{12}$ ($d_{\text{Mn-O}} = 2.124$ and 2.753 Å) [41], which should also explain the dominant role of the A'-O-A' AFM superexchange interaction in $YMn_3Al_4O_{12}$.

VI. CONCLUSIONS

The neutron powder diffraction study has revealed the detailed crystal structure and G-type AFM spin ordering in $YMn_3Al_4O_{12}$. The bond valence sums analysis confirms the $Y^{3+}Mn^{3+}Al^{3+}O^{2-}$ charge state. The crystal and spin structures have also been confirmed by the DFT calculations. Our results illustrate that the magnetic exchange couplings J_1, J_2, and J_3 in $YMn_3Al_4O_{12}$ are all negative (AFM) and that J_1 is much stronger than the others. Therefore, the G-type AFM spin ordering in $YMn_3Al_4O_{12}$ is stabilized almost solely by the NN AFM exchange interaction. From the MLWF tight-binding model analysis, the microscopic mechanism responsible for J_1 has been attributed to (Mn-d_{xy})-(O-p_y)-(Mn-$d_{3z^2-r^2}$) superexchange.

ACKNOWLEDGMENTS

The neutron powder diffraction experiment at the diffractometer D20 (Institut Laue Langevin, France) was done in collaboration with W.-T. Chen (Kyoto University, Japan) and J. P. Attfield and A. Sinclair (The University of Edinburgh, United Kingdom) under the Strategic Japanese-UK Cooperative Program by Japan Science and Technology Agency (JST) and Engineering and Physical Sciences Research Council (ESPRC). The computation in this work has been partly done using the facilities of the Supercomputer Center, the Institute for Solid State Physics, the University of Tokyo. This work was supported by the Core Research for Evolutional Science and Technology (CREST) program of the Japan Science and Technology Agency. The crystallographic figure and schematic views of orbital wave functions were generated using VESTA program [42].

[1] Y. Shimakawa, Inorg. Chem. **47**, 8562 (2008).
[2] The actual symmetry of the 6b sites in $Im\bar{3}$ structure (the A' sites) is not tetragonal $4/mmm$ but orthorhombic mmm.
[3] J. A. Alonso, M. J. Martínez-Lope, M. T. Casais, and M. T. Fernández-Díaz, Inorg. Chem. **39**, 917 (2000).
[4] T. Tohyama, T. Saito, M. Mizumaki, A. Agui, and Y. Shimakawa, Inorg. Chem. **49**, 2492 (2010).
[5] J. B. Goodenough, Phys. Rev. **100**, 564 (1955).
[6] J. Kanamori, J. Phys. Chem. Solids **10**, 87 (1959).
[7] P. W. Anderson, Phys. Rev. **79**, 350 (1950).
[8] A. Muñoz, J. A. Alonso, M. T. Casáis, M. J. Martínez-Lope, J. L. Martínez, and M. T. Fernández-Díaz, J. Phys.: Condens. Matter **14**, 3285 (2002).
[9] D. Okuyama, S. Ishiwata, Y. Takahashi, K. Yamauchi, S. Picozzi, K. Sugimoto, H. Sakai, M. Takata, R. Shimano, Y. Taguchi *et al.*, Phys. Rev. B **84**, 054440 (2011).
[10] H. Li, X. Liu, C. Li, S. Lv, Y. Bai, Z. Wang, and J. Meng, Solid State Sci. **17**, 63 (2013).
[11] G. Zhang, S. Dong, Z. Yan, Y. Guo, Q. Zhang, S. Yunoki, E. Dagotto, and J.-M. Liu, Phys. Rev. B **84**, 174413 (2011).
[12] K. Takata, I. Yamada, M. Azuma, M. Takano, and Y. Shimakawa, Phys. Rev. B **76**, 024429 (2007).
[13] T. Saito, T. Tohyama, P. M. Woodward, and S. Yuichi, Bull. Chem. Soc. Jpn. **84**, 802 (2011).
[14] D. B. Wiles, and R. A. Young, J. Applied Cryst. **14**, 149 (1981).
[15] G. Kresse and J. Hafner, Phys. Rev. B **47**, 558(R) (1993).
[16] G. Kresse and J. Hafner, Phys. Rev. B **49**, 14251 (1994).
[17] G. Kresse and J. Furthmüller, Phys. Rev. B **54**, 11169 (1996).
[18] G. Kresse and J. Furthmüller, Comput. Mat. Sci. **6**, 15 (1996).
[19] P. E. Blöchl, Phys. Rev. B **50**, 17953 (1994).
[20] G. Kresse and D. Joubert, Phys. Rev. B **59**, 1758 (1999).
[21] J. P. Perdew, K. Burke, and M. Ernzerhof, Phys. Rev. Lett. **77**, 3865 (1996).
[22] G. Trimarchi and N. Binggeli, Phys. Rev. B **71**, 035101 (2005).
[23] H. J. Monkhorst and J. D. Pack, Phys. Rev. B **13**, 5188 (1976).
[24] N. Marzari and D. Vanderbilt, Phys. Rev. B **56**, 12847 (1997).
[25] I. Souza, N. Marzari, and D. Vanderbilt, Phys. Rev. B **65**, 035109 (2001).
[26] M. Toyoda, K. Yamauchi, and T. Oguchi, Phys. Rev. B **87**, 224430 (2013).

[27] The orbital labels are defined as follows: Mn-$3d_{3z^2-r^2}$ and O-$2p_z$ are perpendicular to the plaquette. Mn-$3d_{x^2-y^2}$ and O-$2p_x$ have their wave-function lobes directed to the neighboring O and Mn sites.

[28] A. E. Bocquet, T. Mizokawa, T. Saitoh, H. Namatame, and A. Fujimori, Phys. Rev. B **46**, 3771 (1992).

[29] J. H. Jefferson, J. Phys. C: Solid State Phys. **21**, L193 (1988).

[30] T. Sudayama, Y. Wakisaka, T. Mizokawa, H. Wadati, G. A. Sawatzky, D. G. Hawthorn, T. Z. Regier, K. Oka, M. Azuma, and Y. Shimakawa, Phys. Rev. B **83**, 235105 (2011).

[31] T. Kimura, S. Ishihara, H. Shintani, T. Arima, K. T. Takahashi, K. Ishizaka, and Y. Tokura, Phys. Rev. B **68**, 060403(R) (2003).

[32] S. Picozzi, K. Yamauchi, G. Bihlmayer, and S. Blügel, Phys. Rev. B **74**, 094402 (2006).

[33] T. Aoyama, K. Yamauchi, A. Iyama, S. Picozzi, K. Shimizu, and T. Kimura, Nature Commun. **5**, 4927 (2014).

[34] H. Shiraki, T. Saito, T. Yamada, M. Tsujimoto, M. Azuma, H. Kurata, S. Isoda, M. Takano, and Y. Shimakawa, Phys. Rev. B **76**, 140403(R) (2007).

[35] M. Mizumaki, T. Saito, J. Shiraki, and Y. Shimakawa, Inorg. Chem. **48**, 3499 (2009).

[36] P. Kayser, M. Retuero, J. Sánchez-Benítez, M. J. Martínez-Lope, M. T. Fernández-Díaz, and J. A. Alonso, J. Phys.: Condens. Matter **24**, 496002 (2012).

[37] Y. Kim, S. Wakimoto, S. Shapiro, P. Gehring, and A. Ramirez, Solid State Commun. **121**, 625 (2002).

[38] Y. Shimakawa, H. Shiraki, and T. Saito, J. Phys. Soc. Jpn. **77**, 113702 (2008).

[39] Y. Shimakawa and T. Saito, Phys. Status Solidi B **249**, 423 (2012).

[40] T. Saito, M. Toyoda, C. Ritter, S. Zhang, T. Oguchi, J. P. Attfield, and Y. Shimakawa, Phys. Rev. B **90**, 214405 (2014).

[41] S. Zhang, T. Saito, M. Mizumaki, W. T. Chen, T. Tohyama, and Y. Shimakawa, J. Am. Chem. Soc. **135**, 6056 (2013).

[42] K. Momma and F. Izumi, J. Appl. Crystallogr. **44**, 1272 (2011).